Faraday Discussions

This manuscript will be presented and discussed at a forthcoming Faraday Discussion meeting. All delegates can contribute to the discussion which will be included in the final volume.

Register now to attend! Full details of all upcoming meetings: **http://rsc.li/fd-upcoming-meetings**

PAPER

Chemical complexity in the Horsehead Photo-Dissociation Region

Viviana V. Guzmán [a], **Jérôme Pety** [a,b], **Pierre Gratier** [a,b], **Javier R. Goicoechea** [c], **Maryvonne Gerin** [b], **Evelyne Roueff** [d], **Franck Le Petit** [d] and **Jacques Le Bourlot** [d]

The interstellar medium is known to be chemically complex. Organic molecules with up to 11 atoms have been detected in the interstellar medium, and are believed to be formed on the ices around dust grains. The ices can be released into the gas-phase either through thermal desorption, when a newly formed star heats the medium around it and completely evaporates the ices; or through non-thermal desorption mechanisms, such as photodesorption, when a single far-UV photon releases only a few molecules from the ices. The first one dominates in hot cores, hot corinos and strongly UV-illuminated PDRs, while the second one dominates in colder regions, such as low UV-field PDRs. This is the case of the Horsehead were dust temperatures are $\simeq 20 - 30$ K, and therefore offers a clean environment to investigate what is the role of photodesorption. We have carried-out an unbiased spectral line survey at 3, 2 and 1mm with the IRAM-30m telescope in the Horsehead nebula, with an unprecedented combination of bandwidth, high spectral resolution and sensitivity. Two positions were observed: the warm PDR and a cold condensation shielded from the UV field (dense core), located just behind the PDR edge. We summarize our recently published results from this survey and present the first detection of the complex organic molecules HCOOH, CH_2CO, CH_3CHO and CH_3CCH in a PDR. These species together with CH_3CN present enhanced abundances in the PDR compared to the dense core. This suggests that photodesorption is an efficient mechanism to release complex molecules into the gas-phase in far-UV illuminated regions.

1 Introduction

Molecular lines are used to trace the structure of the interstellar medium (ISM) and the physical conditions of the gas in different environments, from high-z galaxies to proto-planetary disks. However, the interpretation of molecular observations for most of these objects is hampered by the complex source geometries, and the small angular sizes in the sky compared with the angular resolution of current instrumentation, that prevent us from resolving the different gas components, and hence to know which specific region each molecule actually traces. Therefore, in order to fully benefit from the diagnostic power of the molecular lines, the formation and destruction paths of the molecules must be quantitatively understood. This challenging task requires the contribution of theoretical models, laboratory experiments and observations. Well-defined sets of observations of simple *template* sources are key to benchmark the predictions of theoretical models. In this respect, the Horsehead nebula has proven to be a good template source of low-UV field irradiated environments because it is close-by (~ 400 pc), it has a simple geometry (edge-on) and its gas density is well constrained. Moreover, in contrast to other Galactic photo-dissociation regions (PDRs), like the Orion Bar and Mon R2 which present large radiation fields ($\chi \simeq 10^4 - 10^5$), the Horsehead is illuminated by a weaker radiation field ($\chi \sim 60$) and thus better resembles the majority of the far-UV illuminated neutral gas in the Galaxy. Furthermore, the dust grains in the Horsehead have temperatures of $\simeq 20 - 30$ K, which is not enough to thermally desorb most of the ices. The Horsehead therefore offers a clean environment to isolate the role of photo-desorption of ices on dust grains.

Observations by the Infrared Space Observatory (ISO) and Spitzer have shown that dust grains are covered by ice mantles in the cold envelopes surrounding high-mass protostars [1,2], low-mass protostars [3–6] and in isolated dense cores [7]. These studies revealed that the ice mantles consist mostly of H_2O, CO_2 and CO, with smaller amounts of CH_3OH, CH_4, NH_3 and H_2CO. More complex prebiotic molecules, such as glycine (NH_2CH_2COOH) could also form on the ices around dust grains. Although their exact formation is unclear, it is believed that the simplest prebiotic molecules have an interstellar origin [8,9]. Indeed, numerous amino acids, which are the building blocks of proteins, have been found in meteorites [10]. In addition, glycine, which is the simplest amino acid, has been

[a] *IRAM, 300 rue de la Piscine, 38406 Saint Martin d'Hères, France. E-mail: guzman@iram.fr*
[b] *LERMA-LRA, UMR 8112, Observatoire de Paris and École normale Supérieure, 24 rue Lhomond, 75231 Paris, France*
[c] *Centro de Astrobiología, CSIC-INTA, Carretera de Ajalvir, Km 4, Torrejón de Ardoz, 28850 Madrid, Spain*
[d] *LUTH UMR 8102, CNRS and Observatoire de Paris, Place J. Janssen, 92195 Meudon Cedex, France*

Table 1 Observation parameters for the maps shown in Figs. 1. The projection center of the maps is $\alpha_{2000} = 05^h40^m54.27^s$, $\delta_{2000} = -02°28'00''$.

Molecule	Transition	Frequency GHz	Instrument	Beam arcsec	PA °	Int. Time hours	T_{sys} K (T_A^*)	Noise K (T_{mb})	Ref.
Continuum at 1.2 mm		250.000000	30m/MAMBO	11.7	–	–	–	–	Hily-Blant et al. [19]
CCH	$1, 3/2(2) - 0, 1/2(1)$	87.316898	PdBI/C&D	7.2×5.0	54				Pety et al. [20]
CH$_3$CHO	$5_{15} - 4_{14}, 6_{16} - 5_{15}$	93.5, 112.2	30m/EMIR	30.0	0				This work
HCO	$1_{01} 3/2, 2 - 0_{00} 1/2, 1$	86.670760	30m/AB100	29.9	0	$2.6/5.0^a$	133	63	Gerin et al. [21]
CF$^+$	$1 - 0$	102.587533	30m/EMIR	25.4	0	2.5	88	0.13	Guzmán et al. [22]
DCO$^+$	$3 - 2$	216.112582	30m/HERA	11.4	0	$1.5/2.0^a$	230	0.10	Pety et al. [23]
p $-$ H$_2$CO	$2_{02} - 1_{01}$	145.602949	30m/EMIR	17.8	0	$7.4/12.9^a$	208	0.17	Guzman et al. [24]
CH$_3$OH $-$ A	$3_0 - 2_0$	145.103152	30m/EMIR	17.9	0	$7.4/12.9^a$	208	0.095	Guzman et al. [24]

^{a} Two values are given for the integration time: the on-source time and the telescope time.
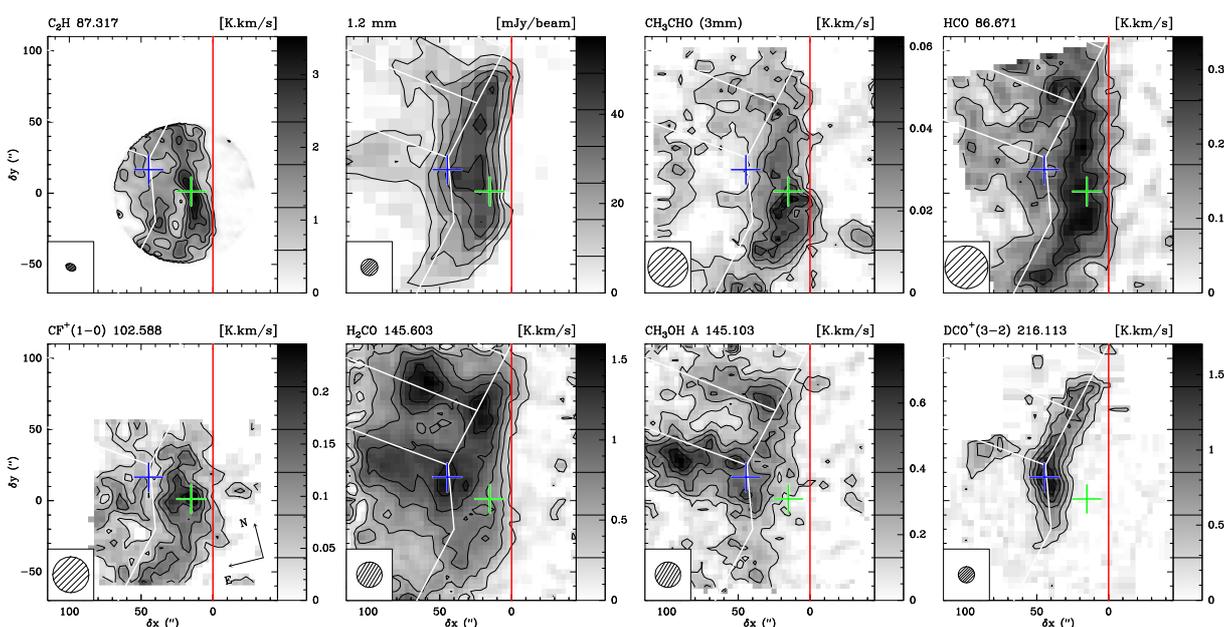
Fig. 1 IRAM-30m and PdBI maps of the Horsehead edge. Maps were rotated by $14°$ counter-clockwise around the projection center, located at $(\delta x, \delta y) = (20'', 0'')$, to bring the exciting star direction in the horizontal direction. The horizontal zero, marked by the red vertical line, delineates the PDR edge. The crosses show the positions of the PDR (green) and the dense core (blue), where deep integrations were performed in the Horsehead WHISPER line survey (PI: J.Pety). The white lines delineate the arc-like structure of the DCO$^+$ emission. The spatial resolution is plotted in the bottom-left corner. Values of contour levels are shown in the respective image lookup table. The emission of all lines is integrated between 10.1 and 11.1 km s^{-1}

detected in samples returned by NASA's Stardust spacecraft from comet Wild 2 [11]. Despite controversial detection claims [12–14], glycine or other more complex amino acids have not been detected in the interstellar medium yet. The most complex molecules detected in the interstellar medium so far, are glycolaldehyde [15] (CH$_2$(OH)CHO), acetamide [16] (CH$_3$CONH$_2$), aminoacetonitrile [17] (NH$_2$CH$_2$CN), and the ethyl formate [18] (C$_2$H$_5$OCHO). This shows the high degree of chemical complexity that can be reached in the interstellar medium.

Simpler, but still complex organic molecules, such as methanol (CH$_3$OH), ketene (CH$_2$CO), acetaldehyde (CH$_3$CHO), formic acid (HCOOH), formamide (NH$_2$CHO), propyne (CH$_3$CCH), methyl formate (HCOOCH$_3$), and dimethyl ether (CH$_3$OCH$_3$), are widely observed in hot cores of high-mass protostars [25–27], and also in hot-corinos of low-mass protostars [28,29]. The complex molecules observed in protostars have been classified in three different generations by Herbst and van Dishoeck [30], depending on their formation mechanism. The zeroth generation species form through grain surface processes in the cold (< 20 K) pre-stellar stage (e.g., H$_2$CO and CH$_3$OH). First generation species form from surface reactions between photodissociated products of the zeroth generation species in the warm-up ($20 - 100$ K) period. Finally, second generations species form in the hot (> 100 K) gas from the evaporated zeroth and first generation species in the so called hot-core phase. Although it is clear that grain surface processes play an important role in the formation of complex molecules, the exact formation mechanism of most complex molecules is still debated.

Bisschop et al. [27] observed several complex molecules toward seven high-mass protostars, and classified them

Table 2 Summary of abundances with respect to total hydrogen nuclei ($N_H = N(X)/(N(H) + 2\,N(H_2))$)) toward the PDR and dense core. The column densities of the total hydrogen nuclei are $N_H = 3.8 \times 10^{22}$ cm^{-2} (PDR) and $N_H = 6.4 \times 10^{22}$ cm^{-2} (dense core).

Species	Beam (″)	PDR Abundance	Offsets	Core Abundance	Offsets	Ref.
C^{18}O	6.5 × 4.3	1.9×10^{-7}	(-6,4)	-	-	Pety et al. [20]
C$_2$H	7.2 × 5.0	1.4×10^{-8}	(-6,4)	-	-	Pety et al. [20]
c-C$_3$H	28	2.7×10^{-10}	(-10,0)	-	-	Teyssier et al. [31]
l-C$_3$H	28	1.4×10^{-10}	(-10,0)	-	-	Teyssier et al. [31]
c-C$_3$H$_2$	6.1 × 4.7	1.1×10^{-9}	(-6,4)	-	-	Pety et al. [20]
l-C$_3$H$_2$	27	$< 4.6 \times 10^{-11}$	(-10,0)	-	-	Teyssier et al. [31]
C$_4$H	6.1 × 4.7	1.0×10^{-9}	(-6,-4)	-	-	Pety et al. [20]
C$_6$H	28	2.2×10^{-11}	(-6,4)	-	-	Agúndez et al. [32]
CS	10	2.0×10^{-9}	(4,0)	2.9×10^{-9}	(21,15)	Goicoechea et al. [33]
C^{34}S	16	9.2×10^{-11}	(4,0)	9.1×10^{-11}	(21,15)	Goicoechea et al. [33]
HCS$^+$	29	1.7×10^{-11}	(4,0)	1.2×10^{-11}	(21,15)	Goicoechea et al. [33]
HCO	6.7 × 4.4	8.4×10^{-10}	(-5,0)	$< 8.0 \times 10^{-11}$	(20,22)	Gerin et al. [21]
HCO$^+$	28	9.0×10^{-10}	(-5,0)	3.9×10^{-9}	(20,22)	Goicoechea et al. [34]
H^{13}CO$^+$	6.8 × 4.7	1.5×10^{-11}	(-5,0)	6.5×10^{-11}	(20,22)	Goicoechea et al. [34]
HOC$^+$	28	4.0×10^{-12}	(-5,0)	-	(20,22)	Goicoechea et al. [34]
CO$^+$	10	$< 5.0 \times 10^{-13}$	(-5,0)	-	(20,22)	Goicoechea et al. [34]
DCO$^+$	12	-	(-5,0)	8.0×10^{-11}	(20,22)	Pety et al. [23]
CF$^+$	25	5.7×10^{-10}	(-5,0)	$< 6.9 \times 10^{-11}$	(20,22)	Guzmán et al. [22]
C$_3$H$^+$	27	3.1×10^{-11}	(-5,0)	-	(20,22)	Pety et al. [35]
o $-$ H$_2$CO	6.1 × 5.6	1.9×10^{-10}	(-5,0)	1.5×10^{-10}	(20,22)	Guzmán et al. [36]
p $-$ H$_2$CO	6.1 × 5.6	9.5×10^{-11}	(-5,0)	5.0×10^{-11}	(20,22)	Guzmán et al. [36]
HDCO	18	-	(-5,0)	2.5×10^{-11}	(20,22)	Guzmán et al. [36]
D$_2$CO	24	-	(-5,0)	1.6×10^{-11}	(20,22)	Guzmán et al. [36]
CH$_3$OH $-$ E	6.1 × 5.6	7.0×10^{-11}	(-5,0)	1.0×10^{-10}	(20,22)	Guzman et al. [24]
CH$_3$OH $-$ A	6.1 × 5.6	5.3×10^{-11}	(-5,0)	1.3×10^{-10}	(20,22)	Guzman et al. [24]
CH$_3$CN	27	2.5×10^{-10}	(-5,0)	7.9×10^{-12}	(20,22)	Gratier et al. [37]
CH$_3$NC	25	4.1×10^{-11}	(-5,0)	$< 7.8 \times 10^{-12}$	(20,22)	Gratier et al. [37]
HC$_3$N	30	6.3×10^{-12}	(-5,0)	7.9×10^{-12}	(20,22)	Gratier et al. [37]
t $-$ HCOOH	29	5.2×10^{-11}	(-5,0)	1.4×10^{-11}	(20,22)	This work
o $-$ CH$_2$CO	30	1.3×10^{-10}	(-5,0)	4.2×10^{-11}	(20,22)	This work
p $-$ CH$_2$CO	26	1.8×10^{-11}	(-5,0)	7.3×10^{-12}	(20,22)	This work
CH$_3$CHO $-$ E	27	1.4×10^{-11}	(-5,0)	3.9×10^{-12}	(20,22)	This work
CH$_3$CHO $-$ A	27	5.4×10^{-11}	(-5,0)	2.0×10^{-11}	(20,22)	This work
CH$_3$CCH	29	4.4×10^{-10}	(-5,0)	3.0×10^{-10}	(20,22)	This work

as cold (T< 100 K) and hot (T> 100 K) molecules based on their rotational temperatures. The hot molecules include H$_2$CO, CH$_3$OH, HNCO, CH$_3$CN, HCOOCH$_3$ and CH$_3$OCH$_3$, while the cold molecules include HCOOH, CH$_2$CO, CH$_3$CHO, and CH$_3$CCH. The cold molecules are expected to be present in the colder envelope around the hot-core. Öberg et al. [38] studied the spatial distribution of complex molecules around a high-mass protostar and found that CH$_2$CO, CH$_3$CHO and CH$_3$CCH are indeed abundant in the cold envelope. They classified them as zeroth order molecules because their formation must require very little heat.

Complex organic molecules may trace other environments than hot cores and hot corinos. They are also present in the cold UV-shielded gas. Bacmann et al. [39] detected CH$_3$OCH$_3$, CH$_3$OCHO, CH$_2$CO and CH$_3$CHO in a cold ($T_{kin} \sim 10$ K) prestellar core. These observations challenged the current formation scenario of complex molecules on dust grains, because the diffusion reactions that lead to the formation of species are not efficient on dust grains with temperatures of ~ 10 K. CH$_3$CHO and CH$_2$CO have also been detected in the dark cloud TMC-1 [40,41]. CH$_2$CO and CH$_3$CHO have also been detected in a $z = 0.89$ spiral galaxy located in front of the quasar PKS1830-211 [42].

In this paper, we present the results of an unbiased line survey performed with the IRAM-30m telescope in a classic star forming region, the Horsehead nebula. We describe the observations in section 2. In section 3 we present a summary of the recently published results of the line survey. In section 4 we present new unpublished

results about the first detection of complex molecules in a PDR. We discuss these observations in section 5 and conclude in section 6

2 Observations

2.1 Deep pointed integrations: The Horsehead WHISPER line survey

With the purpose of providing a benchmark to chemical models we have performed a complete and unbiased line survey: the Horsehead WHISPER (Wideband High-resolution Iram-30m Surveys at two Positions with Emir Receivers, PI: J. Pety). Two positions were observed: 1) the HCO peak, which is characteristic of the photo-dissociation region at the surface of the Horsehead nebula[21], and 2) the DCO^+ peak, which belongs to a cold condensation located less than $40''$ away from the PDR edge, where HCO^+ and other species are highly deuterated[23]. Hereafter we refer to these two positions as the PDR and dense core, respectively. The combination of the new EMIR receivers at the IRAM-30m telescope and the Fourier transform spectrometers (FTS) yields a spectral survey with unprecedented combination of bandwidth (36 GHz at 3mm, 34 GHz at 2mm and 73 GHz at 1mm), spectral resolution (49 kHz at 3 and 2mm; and 195 kHz at 1mm), and sensitivity (median noise 8.1 mK, 18.5 mK and 8.6 mK at 3, 2 ans 1mm respectively). A detailed presentation of the observing strategy and data reduction process will be given in a forthcoming paper. In short, all frequencies were observed with two different frequency tunings and the Horsehead PDR and dense core positions were alternatively observed every 15 minutes in position-switching mode with a common fixed off-position. This observing strategy allows us to remove potential ghost lines that are incompletely rejected from a strong line in the image sideband (the typical rejection of the EMIR sideband-separating mixers is only 13dB).

The line density at 3 mm is, on average, 5 and 4 lines/GHz in the PDR and dense core, respectively. At 2 and 1 mm, the line density is 1 line/GHz in both the PDR and dense core. The contribution of molecular lines to the total flux at 1.2 mm is estimated to be 14% at the PDR and 16% at the dense core. Approximately 30 species (plus their isotopologues) are detected with up to 7 atoms in the PDR and the dense core.

2.2 IRAM-30m and PdBI maps

Figure 1 displays the integrated emission of the C_2H, CH_3CHO, HCO, CF^+, DCO^+, $p-H_2CO$, and CH_3OH-A lines as well as the 1.2mm continuum emission. The observation parameters are summarized in Table 1. A reference is given where a detailed description of the observations and data reduction can be found for each map.

The A- and E-type CH_3CHO $5_{15}-4_{14}$ lines at 93.581 GHz and 93.595 GHz were observed simultaneously with the A- and E-type CH_3CHO $6_{16}-5_{15}$ lines at 112.249 GHz and 112.254 GHz during telescope time ~ 17 hours of average summer weather in August and September 2013. We used the two polarizations of the EMIR receivers and the FTS backends at 49 kHz spectral resolution. We used the position-switching, on-the-fly observing mode. The off-position offsets were $(\delta RA, \delta Dec) = (100'', 0'')$, that is, the H II region ionized by σOri and free of molecular emission. We observed along and perpendicular to the direction of the exciting star in zigzags (i.e., $\pm$ the lambda and beta scanning direction). From our knowledge of the IRAM-30m telescope, we estimate the absolute position accuracy to be $3''$.

The IRAM-30m data were processed with the `GILDAS/CLASS` software. The data were first calibrated to the T_A^* scale using the chopper-wheel method[43]. The data were converted to main-beam temperatures (T_{mb}) using the forward and main-beam efficiencies (F_{eff} and B_{eff}). The resulting amplitude accuracy is 10%. We then computed the experimental noise by subtracting a zeroth-order baseline from every spectra. A systematic comparison of this noise value with the theoretical noise computed from the system temperature, the integration time, and the channel width allowed us to filter out outlier spectra. The spectra where then gridded to a data cube through a convolution with a Gaussian kernel. In order to increase the signal-to-noise ratio, we smoothed the four A- and E-type CH_3CHO lines to the largest angular resolution and then averaged all the data. The averaged map, which has a final resolution of $30''$, is shown in Fig 1.

3 Recent results from the Horsehead WHISPER line survey

3.1 CF^+: a tracer of C^+ and a measure of the fluorine abundance

CF^+, which was only detected in the Orion Bar before[44], was detected toward the illuminated edge of the Horsehead nebula by Guzmán et al.[22]. The CF^+ ion, which is formed by reactions of HF and C^+, is expected to be the second most important fluorine reservoir, after HF, in regions where C^+ is abundant[45]. Indeed, the CF^+ emission is concentrated toward the edge of the Horsehead, delineating the western edge of the DCO^+ emission (see Fig. 1). Theoretical models predict that there is a significant overlap between CF^+ and C^+ at the edges of molecular clouds.

Therefore, we propose that CF^+ can be used as a proxy of C^+, but that can be observed from ground-based telescopes, unlike C^+ for which we need to go to space. This can be a powerful tool, because the [C II] 157.8 μm line is the main cooling mechanism of the diffuse gas, and the cooling of the medium, which allows the gas to compress, is a crucial step in the formation of new stars. Moreover, given the simple chemistry of fluorine and assuming that the CF^+ destruction is dominated by dissociative recombination with electrons with little contribution from photodissociation (which is true only in low-UV PDRs), one obtains that the CF^+ column density is proportional to the column density of HF. Then, assuming that in molecular clouds all fluorine is in its molecular form, the elemental abundance of fluorine can be derived directly from CF^+ observations. We infer F/H$= (0.6 - 1.5) \times 10^{-8}$ in good agreement with the one found in diffuse molecular clouds[46], and somewhat lower than the solar value[47] and the one found in the diffuse atomic gas[48]. Finally, because the Horsehead shows narrow emission lines, in contrast to other PDRs like the Orion Bar, Guzmán *et al.*[49] were able to resolve the two hyperfine components in the CF^+ $J = 1 - 0$ line and to compare with *ab initio* computations of the CF^+ spin rotation constant. The derived theoretical value of $C_I = 229.2$ kHz agrees well with the observations. The Horsehead is thus a good laboratory for precise spectroscopic studies of species present in far-UV illuminated environments.

3.2 Detection of a new molecule in space, tentatively attributed to l-C_3H^+

Thanks to the sensitive observations and large bandwidth covered by the Horsehead WHISPER line survey, a consistent set of 8 lines were detected toward the PDR position, that could not be associated to any transition listed in the public line catalogs. The observed lines can be well fitted with a linear rotor model, implying a closed-shell molecule. The deduced rotational constant value is close to that of C_3H. In addition, the spatial distribution of the species integrated emission has a shape similar to radical species such as HCO, and small hydrocarbons such as C_2H (see Fig. 1). Therefore, Pety *et al.*[35] attributed the detected lines to the small hydrocarbon cation l-C_3H^+.

In the family of small hydrocarbons, Pety *et al.*[20] found that C_3H and C_3H_2 are about 1 order of magnitude more abundant in PDRs than current pure gas-phase models predict. An additional formation mechanism is therefore needed. One possibility to explain the observed high abundance of hydrocarbons in PDRs is the so called *Top-Down* model. In this scenario polycyclic aromatic hydrocarbons (PAHs) are fragmented into small hydrocarbons in PDRs due to the strong UV fields[20,31,50]. In the same way, PAHs are formed by photo-evaporation of very small grains[51,52]. The discovery of C_3H^+, which is an intermediate species in the gas-phase formation scenario, brings further constraints to the formation pathways of the small hydrocarbons. Indeed, we find a l-C_3H^+ abundance which is too low to explain the observed abundance of the other related small hydrocarbons by means of pure gas-phase chemical reactions.

The lines detected in the Horsehead have been detected in other environments, like the Orion Bar (Cuadrado et al. in prep) and Sgr B2[53], which confirms the presence of the carrier in the ISM. But the attribution of the unidentified lines to l-C_3H^+ has been questioned by Huang *et al.*[54], because their theoretical calculations of the spectroscopic constants of C_3H^+ differ from the ones inferred from our observations. Fortenberry *et al.*[55] proposed that a more plausible candidate is the hydrocarbon anion C_3H^-. However, if the unknown species is the anion, it would be the first anion detected in the Horsehead, and the ratio of C_3H^- to neutral C_3H would be $\sim 57\%$, which is higher than any anion to neutral ratio detected in the ISM so far. In addition, the lines were not detected in the dark cloud TMC 1, where other anions have been already detected. Moreover, because C_3H^- is an asymmetric rotor, the lines detected in the Horsehead would correspond to the $K_a = 0$ ladder and the lines from the $K_a = 1$ ladder should also be detected. We find no evidence of the $K_a = 1$ lines of C_3H in the observations of the Horsehead PDR (McGuire *et al. 2013, accepted to ApJ*). For all these reasons it would be unexpected that the carrier of the unidentified lines is the anion, C_3H^-. The observations favor the assignment of the unidentified species to the hydrocarbon cation, C_3H^+, as the most likely candidate. However, A direct measurement in the laboratory is necessary to provide a definitive answer and close the controversy created by these observations in the Horsehead. Ongoing high-angular PdBI observations of this species in the Horsehead PDR will allow us to better constrain the chemistry of small hydrocarbons in the near future.

3.3 Photo-desorption of dust grain ice mantles: H_2CO and CH_3OH

Relatively simple organic molecules, like H_2CO and CH_3OH, are key species in the synthesis of more complex molecules in the ISM[56–58], that could eventually end up in proto-planetary disks, and hence in new planetary systems. They are also used to probe the temperature and density of the gas in different astrophysical sources[59–61]. Both H_2CO and CH_3OH have been detected in a wide range of interstellar environments such as dark clouds, proto-stellar cores and comets, with high abundances ($10^{-6} - 10^{-9}$) with respect to total hydrogen. Unlike H_2CO, which can be formed efficiently in both the gas-phase and on the surfaces of dust grains, CH_3OH is thought to be formed mostly on the ices, through the successive additions of hydrogen atoms to adsorbed CO molecules.

Guzmán *et al.*[36] and Guzman *et al.*[24] observed several millimeter lines of H_2CO and CH_3OH toward the PDR and dense core positions in the Horsehead. The inferred abundances from the observations (see Table 2)
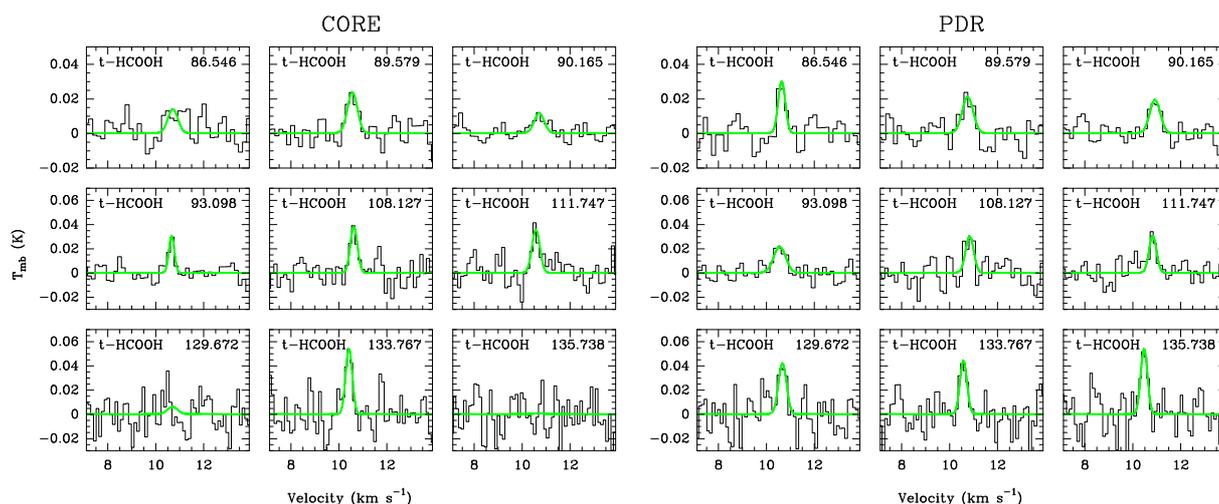
Fig. 2 HCOOH lines detected toward the dense core (*left*) and PDR (*right*). For each line, the same scale is used at both positions to ease the comparison.
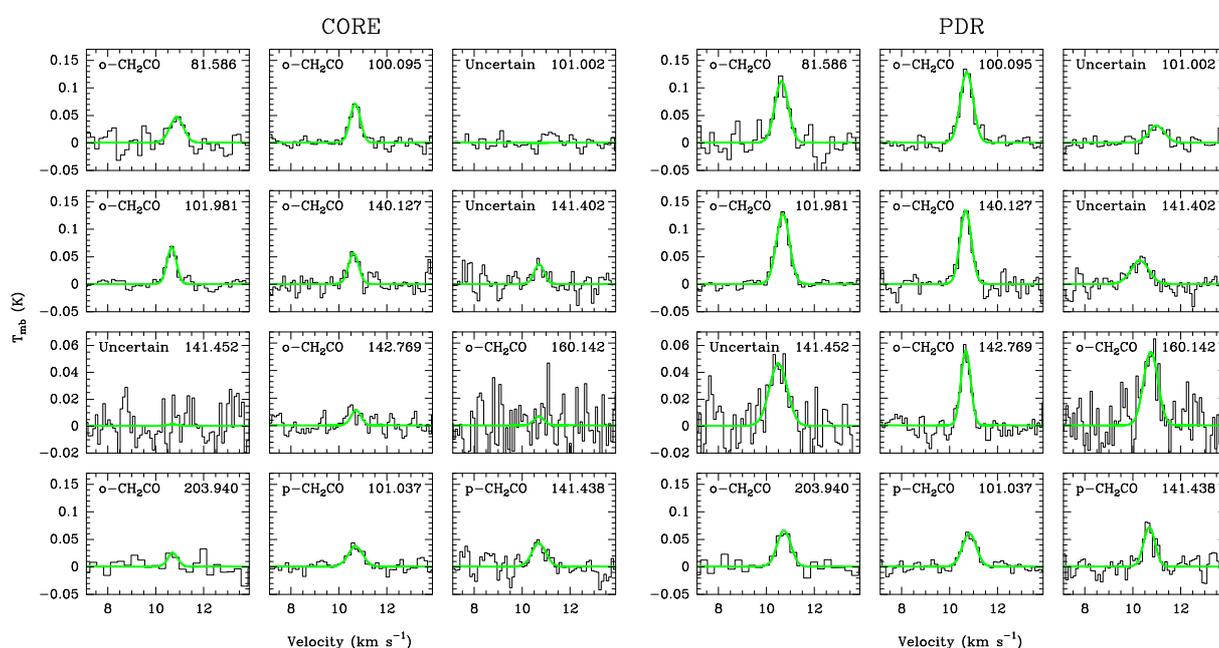
Fig. 3 CH$_2$CO lines detected toward the dense core (*left*) and PDR (*right*). For each line, the same scale is used at both positions to ease the comparison.

were compared to PDR models that include either pure gas-phase chemistry or both gas-phase and grain surface chemistry. Pure gas-phase models cannot reproduce the observed abundances of either H$_2$CO or CH$_3$OH at the PDR position. Both species are therefore mostly formed on the surface of dust grains, probably through the successive hydrogenation of CO ices and are subsequently released into the gas-phase through photodesorption. At the dense core, on the other hand, photodesorption of ices is needed to explain the observed abundance of CH$_3$OH, while a pure gas-phase model can reproduce the observed H$_2$CO abundance. The different formation routes for H$_2$CO at the PDR and dense core suggested by the models is strengthened by the different ortho-to-para ratios derived from the observations (~ 3 at the dense core, ~ 2 at the PDR).

In addition to the lines detected in the WHISPER survey, we obtained high-angular resolution (6″) maps of H$_2$CO and CH$_3$OH with the IRAM-PdBI. Fig. 1 shows the H$_2$CO and CH$_3$OH single-dish 30m maps that were used for the short-spacing of the PdBI observations. The H$_2$CO emission map presents a peak at the dense core position, while CH$_3$OH presents a dip in its emission at the same position. The observations thus suggest that CH$_3$OH is depleted in the dense core. This way, gas-phase CH$_3$OH is present in an envelope around the dense core, while H$_2$CO is present in both the envelope and the dense core itself. Indeed, we expect photodesorption to be more efficient at the PDR than at the far-UV shielded dense core. We thus conclude that photo-desorption of

CORE   PDR
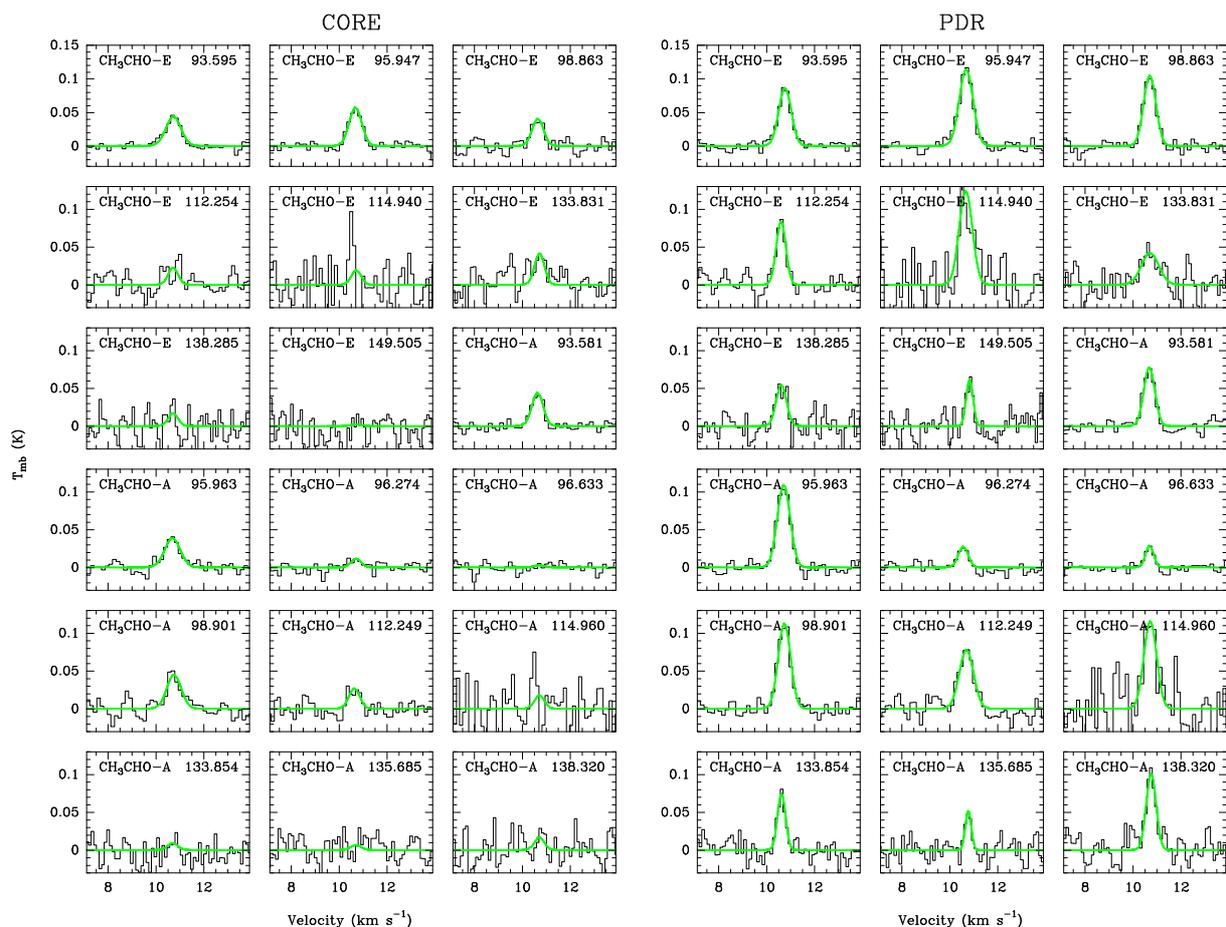
Fig. 4 CH$_3$CHO lines detected toward the dense core (*left*) and PDR (*right*). For each line, the same scale is used at both positions to ease the comparison.

CORE   PDR
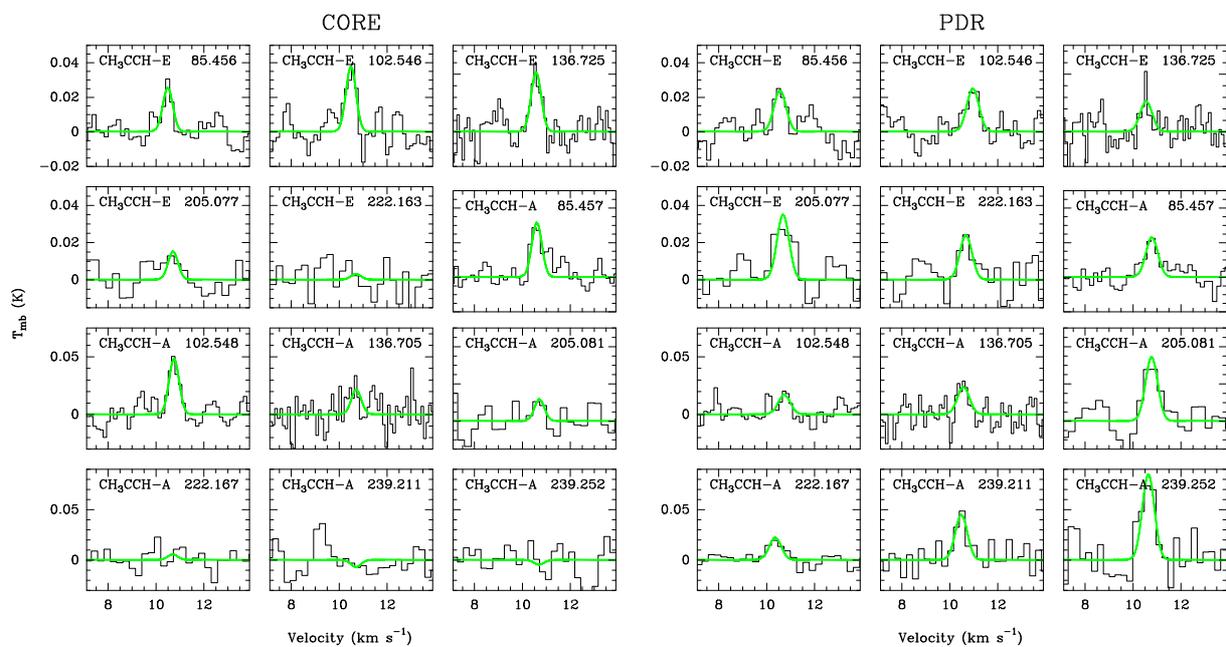
Fig. 5 CH$_3$CCH lines detected toward the dense core (*left*) and PDR (*right*). For each line, the same scale is used at both positions to ease the comparison.

ices is an efficient mechanism to release species into the gas-phase in far-UV illuminated regions.

3.4 Nitrile molecules: CH₃CN, CH₃NC and HC₃N

Moderately complex nitriles like CH$_3$CN and HC$_3$N are easily detected in (massive) star forming regions. In particular, the CH$_3$CN emission has been found to be enhanced in star forming regions containing an ultracompact H II region[62]. CH$_3$CN is thought to be a good tracer of the physical conditions in warm and dense regions. Gratier *et al.*[37] detected several lines of CH$_3$CN and HC$_3$N in the PDR and dense core. CH$_3$NC and C$_3$N are also detected toward the PDR. The observations show that the chemistry of HC$_3$N and CH$_3$CN is quite different. Indeed, we find that CH$_3$CN is 30 times more abundant in the far-UV illuminated gas than in the far-UV shielded core, while HC$_3$N has a similar abundance in both positions. The high abundance of CH$_3$CN inferred in the PDR is surprising because the photodissociation of this complex molecule is expected to be efficient in far-UV illuminated regions. The observed abundance in the PDR cannot be reproduced by current pure gas-phase chemical models. We have shown that photodesorption is an efficient mechanism to release H$_2$CO and CH$_3$OH in the PDR, but the case of CH$_3$CN is even more extreme as it is 30 times more abundant there than in the dense core, while H$_2$CO presents similar abundances in both positions. This shows that there is something specific in the chemistry of CH$_3$CN in FUV-illuminated regions. CH$_3$CN could be produced on the ices by the photo-processing of N bearing species followed by photodesorption, but it could also be produced in the gas-phase if the abundances of its gas-phase precursors, HCN and CH$_3^+$, are enhanced. The detection of CH$_3$NC at the PDR, which results in an CH$_3$NC/CH$_3$CN isomeric ratio of 0.15, suggests that CH$_3$NC could also form on the surfaces of dust grains through far-UV irradiation of CH$_3$CN ices leading to isomerization.

4 Other complex molecules in PDRs

Within the WHISPER line survey, several lines of HCOOH, CH$_2$CO, CH$_3$CHO and CH$_3$CCH are detected. These are presented in Figs. 2 to 3. The spectroscopic parameters and Gaussian fit results of the detected lines are listed in Appendix A. The spectroscopic parameters are taken from the CDMS[63] and JPL[64] data bases. Several lines of ketene and acetaldehyde are clearly detected ($S/N > 5\sigma$). The formic acid and propyne present several but fainter ($2\sigma - 5\sigma$) lines toward the PDR and dense core positions. In order to confirm the correct identification of these molecules, we have modeled the spectrum of each species assuming LTE and optically thin emission, and checked that there are no predicted lines missing in the line survey. Both ortho and para forms of CH$_2$CO are detected, as well as both E and A forms of CH$_3$CHO and CH$_3$CCH. All the lines detected of the formic acid correspond to the trans isomer. CH$_2$CO, CH$_3$CHO lines are brighter toward the PDR position than toward the dense core, while HCOOH and CH$_3$CCH lines have similar brightness in both positions.

The beam-averaged column density of each molecule was estimated using rotational diagrams because no collisional coefficients are available. The detected lines cover a sufficiently large energy range to derive a rotational temperature. The resulting rotational diagrams are shown in Fig. 6. The inferred abundances with respect to H nuclei are summarized in Table 2. The partition function was computed independently for ortho and para nuclear spin forms (for ketene), and for E and A symmetry forms (for CH$_3$CHO), by direct summation over the energy levels.

Formic acid

The data in the rotational diagram of HCOOH present a large scatter because all the detected lines are weak and therefore have a larger uncertainty than the lines of the other complex molecules. The rotational temperature is poorly constrained. The inferred abundances of $\sim 5 \times 10^{-11}$ (PDR) and $\sim 1 \times 10^{-11}$ (core) are thus also uncertain and should be considered as an order of magnitude estimate. Deeper integration times are needed to better constrain the HCOOH abundance.

Ketene

The ortho and para symmetries of CH$_2$CO were treated as different species. When including all the o$-$CH$_2$CO and p$-$CH$_2$CO lines detected in the PDR, the fit results in rotational temperatures of 154 K and 120 K for o$-$CH$_2$CO and p$-$CH$_2$CO, respectively. These temperatures are much larger than the kinetic temperature at the PDR ($\sim$60 K). When the three lines of CH$_2$CO with energies above 80 K that are detected at the PDR (gray points in Fig. 6) are not considered in the rotational diagrams, the derived rotational temperatures decrease to 18 K for both ortho and para species. This temperature agrees much better with the expected sub-thermal excitation in the Horsehead, and also with the derived rotational temperatures at the dense core. The enhanced emission of the three lines with $E_u > 80$ K could be the result of an excitation effect. However, these lines are broader (0.8 km s^{-1}) than the other CH$_2$CO lines and than other species detected in the Horsehead PDR (the typical linewidth is 0.6 km s^{-1}). In addition, the velocity of these three lines differs by 0.2 km s^{-1} from the systemic velocity of 10.7 km s^{-1} found for most species in the Horsehead. Cummins *et al.*[25] detected several o$-$CH$_2$CO

Table 3 Dipole moments of complex molecules

Species	Dipole moment (Debye)	Reference
HCOOH	1.4	Kim *et al.* [65]
CH_2CO	1.45	Hannay and Smyth [66]
CH_3CHO	2.7	Kleiner *et al.* [67]
CH_3CCH	0.78	Burrell *et al.* [68]

lines toward Sgr B2, including the $5_{33} - 4_{32}$ at 101.002 GHz, which is one of the three lines detected in the Horsehead with $E_u > 80$ K. They also obtained a large rotational temperature, which led them to remove this line from the fit and consider the identification as uncertain. At the dense core position in the Horsehead, the derived rotational temperature for $o-CH_2CO$ is ~ 14 K. Only two lines of $p-CH_2CO$ are detected at the dense core, resulting in a rotational temperature of ~ 20 K. Ketene is ~ 3 times more abundant in the PDR than in the dense core, with abundances of 1.5×10^{-10} (PDR) and 4.9×10^{-11} (core). The ortho-to-para ratio is poorly constrained, resulting in $o/p = 7.1 \pm 4.2$ (PDR) and $o/p = 5.7 \pm 3.9$ (dense core).

Acetaldehyde

The E and A symmetries of CH_3CHO were also treated as different species. Acetaldehyde has a large dipole moment (2.7 Debye, see Table 3) compared to methanol (1.7 Debye). Since the critical density is proportional to μ^2, sub-thermal effects are important for CH_3CHO[27]. Indeed, the derived rotational temperatures for CH_3CHO ($6-10$ K) are the lowest ones of all the molecules discussed here. The derived column density of CH_3CHO is ~ 3 times larger in the PDR than in the dense core. The inferred E/A ratio is $\sim 0.3 \pm 0.1$ (PDR) and $\sim 0.2 \pm 0.2$ (core), *i.e.*, much lower than unity in both positions.

Figure 1 displays the averaged E and A CH_3CHO lines at 93.6 GHz. The CH_3CHO emission clearly peaks at the PDR position, delineating the edge of the Horsehead nebula. The CH_3CHO emission resembles the HCO emission at the 30m telescope angular resolution of $30''$, which is concentrated in a narrow structure peaking at the PDR. Higher-angular resolution ($6''$) observations by Gerin *et al.*[21] showed that the HCO emission traces a filament of $\sim 12''$ width. The similarities between the emission of HCO and CH_3CHO thus suggest that CH_3CHO also arises from a narrow filament that peaks at the PDR position. Assuming a filament of $12''$ centered at the PDR, we estimate that $\sim 10\%$ of the CH_3CHO emission detected at the dense core corresponds to beam pick-up from the PDR due to the large beam at 93 GHz ($27''$). The remaining emission towards the core line of sight could arise from the cloud surface, as was found for CS[33] and HCO.[21]

Propyne

If CH_3CCH-E and CH_3CCH-A are treated as different species, the derived rotational temperatures at the PDR are ~ 70 K and ~ 53 K for E and A symmetries, respectively. At the dense core, a rotational temperature of ~ 70 K is inferred for the E symmetry. A rotational temperature cannot be inferred for CH_3CCH-A at the dense core because the two lines that are detected are faint. The two symmetries are therefore considered as the same species, resulting in a rotational temperature of ~ 55 K and a total column density for the E- and A-type CH_3CCH of $\sim 2 \times 10^{13}$ cm^{-2} at both the PDR and dense core position. The inferred column density at the PDR position does not change when the E and A symmetries are separated.

5 Discussion

Ketene and acetaldehyde are thought to form on the surface of dust grains. Indeed, CH_3CHO has been proposed as a candidate for the 7.41 μm absorption feature observed toward high-mass protostars. Ketene and acetaldehyde are thought to form together on the ices through C and H atom additions to CO[30]. The expected sequence is

$$CO \xrightarrow{H} HCO \xrightarrow{C} HCCO \xrightarrow{H} CH_2CO \xrightarrow{2H} CH_3CHO. \tag{1}$$

Ketene can also be formed from reactions between C_2H_2 and O in irradiated H_2O-rich and CO_2-rich ices, as shown by recent laboratory experiments[69]. Laboratory experiments also show that reactions between C_2H_4 and O can produce acetaldehyde and its isomer, ethylene oxide (CH_2OCH_2)[70]. CH_2CO and CH_3CHO could also be formed in the gas-phase, through ion-molecule and neutral-neutral reactions. Indeed, gas-phase models predict abundances that are comparable to those measured in some of the high-mass protostars observed by Bisschop *et al.*[27].
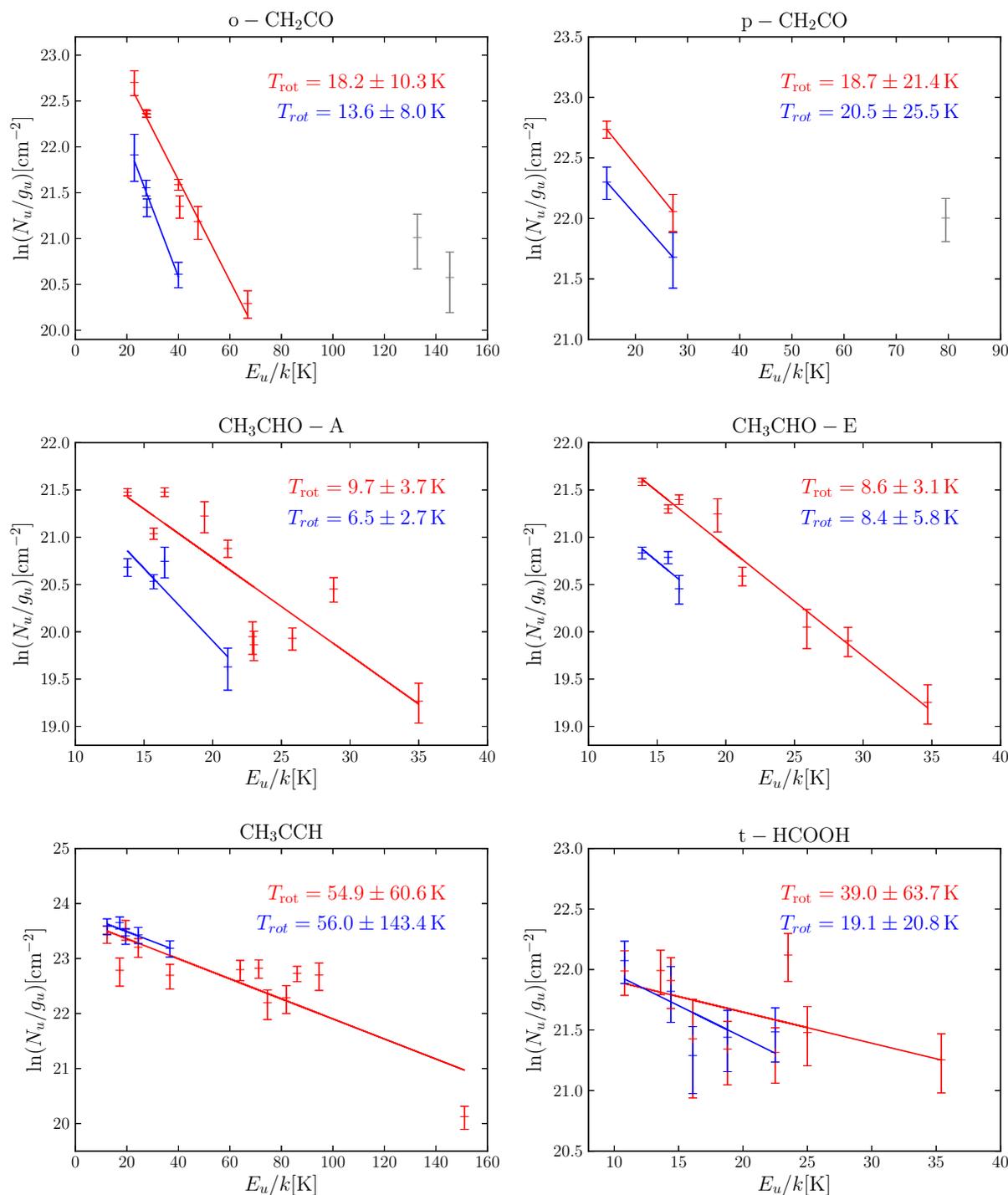
Fig. 6 Rotational diagrams for the PDR (red) and dense core (blue). The gray points correspond to the three lines detected at the PDR whose identification is uncertain. They are not considered in the fit.

The exact formation path of HCOOH on ices is unclear, though HCOOH ices have been observed in star-forming regions[71]. Several formation paths on grain surfaces have been proposed in the past. It could form from the addition of H and O atoms to CO or to CO_2[72]. Garrod *et al.*[73] proposed that HCOOH could form through reactions between HCO and OH. More recently, Ioppolo *et al.*[74] have studied the hydrogenation of the HO-CO complex in the laboratory and showed it is an efficient formation route to HCOOH.

The abundances derived in the Horsehead PDR for HCOOH, CH_2CO, and CH_3CHO, are $3-4$ times larger toward the PDR than toward the dense core. The case of CH_3CN is even more extreme as it is ~ 30 times more abundant in the PDR than in the dense core[37]. CH_3CCH is only 1.5 times more abundant in the PDR than in the dense core. In contrast, methanol is ~ 2 times *less* abundant in the PDR than in the dense core. When comparing
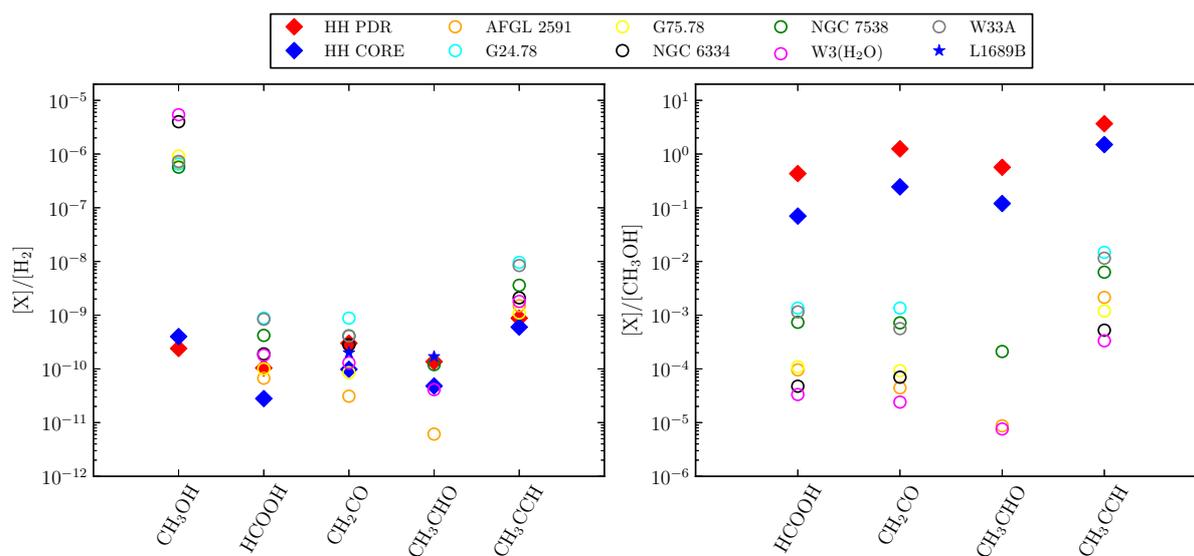
Fig. 7 Abundances with respect to H$_2$ (*left*) and with respect to CH$_3$OH (*right*) toward the hot core sources from Bisschop *et al.*[27] (*open circles*), the cold prestellar core from Bacmann *et al.*[39] (*blue star*) and the Horsehead PDR and dense core (*red and blue diamonds*).

the abundances of the different molecules, we found that CH$_3$CCH is one order of magnitude more abundant ($3 - 4 \times 10^{-10}$) than CH$_2$CO and CH$_3$CHO ($2 - 7 \times 10^{-11}$). Contrary to the other complex molecules, which present [X]/[CH$_3$OH] ratios lower than 1, CH$_3$CCH is ~ 4 times more abundant than methanol in the PDR, and ~ 1.3 times more abundant than methanol in the dense core. Öberg *et al.*[38] also found large CH$_3$CCH abundances (~ 1 relative to methanol) toward the high-mass protostar NGC 7538 IRS9. They found the CH$_3$CCH/CH$_3$OH abundance ratio to be significantly different to what models including grain surface processes predict, which suggests that an important cold formation pathway is missing for CH$_3$CCH.

Fig. 7 shows a comparison between the abundances derived in the Horsehead and those derived toward the hot corino sources from Bisschop *et al.*[27] and toward the prestellar core L1689B[39]. CH$_3$OH is several orders of magnitude more abundant toward the hot core sources than in the Horsehead. The abundances of the other complex molecules with respect to H$_2$ vary over ~ 1 order of magnitude between the different hot core sources, and are comparable to the abundances derived in the Horsehead. The abundances with respect to CH$_3$OH are also shown in the right panel of Fig. 7. In this case, the abundances of complex molecules are ~ 3 orders of magnitude larger in the Horsehead than in the hot cores. However, this could be a consequence of methanol and the other complex molecules tracing different regions in the hot core sources. Methanol probably traces the hot ($T_{kin} > 100$ K) gas where species have evaporated from the grains, while the other complex molecules trace the colder envelope around the protostars, where the ices have not completely evaporated but can be photodesorbed.

The fact that we only detect cold molecules (HCOOH, CH$_2$CO, CH$_3$CHO and CH$_3$CCH) and none of the hot molecules (e.g., CH$_3$OCH$_3$ and HCOOCH$_3$), is in agreement with the idea that the cold molecules are zeroth or first generation species formed on the cold grain surfaces and trace the warm/cold envelope around protostars, because their formation probably requires little energy. In the Horsehead, the enhanced abundances toward the PDR compared to the dense core (for HCOOH, CH$_2$CO, and CH$_3$CHO), suggests that their formation is more efficient in the presence of far-UV photons. The similarities between the HCO and CH$_3$CHO emission maps also suggests that the CH$_3$CHO abundance at the PDR could be even higher than estimated here, if the emission arises from a narrow filament like HCO. This could be the result of an efficient photodesorption in the PDR, due to the larger radiation field compared to the dense core, which is consistent with the much lower than unity E/A ratio (statistical value) we infer from the observations. But it could also indicate that the formation on the grains itself is more efficient in the PDR, due to a better mobility of the molecules in ice mantles. Indeed, recent laboratories experiments have shown that the diffusion of molecules is active at $T_{dust} \gtrsim 30$ K, allowing reactions to proceed faster when the ices are warmed by far-UV photons[75,76]. Dust temperatures in the Horsehead PDR range from $T_{dust} \sim 30$ K in the PDR to $T_{dust} \sim 20$ K in the dense core[77].

6   Conclusions

We have carried-out an unbiased spectral line survey at 3, 2 and 1mm with the IRAM-30m telescope in the Horse-head nebula, with an unprecedented combination of bandwidth, high spectral resolution and sensitivity. Two positions were observed: the warm photodissociation region (PDR) and a cold condensation shielded from the UV field, located less than $40''$ away from the PDR edge. The results of this survey include 1) the detection of CF^+, which can be used as a new diagnostic of UV illuminated gas and a potential proxy of the C^+ emission associated to molecular gas; 2) the detection of a new species in the ISM, tentatively attributed to C_3H^+, which confirms the top-down scenario of formation of the small hydrocarbons from PAHs and photo-erosion; 3) the detection of H_2CO, CH_3OH and CH_3CN, which reveals that photo-desorption of ices is an efficient mechanism to release molecules into the gas phase; 4) and the first detection of the complex organic molecules, HCOOH, CH_2CO, CH_3CHO and CH_3CCH in a PDR, which reveals the degree of chemical complexity reached in the UV illuminated neutral gas. Complex molecules are usually considered as hot-core tracers. The detection of these molecules in PDRs shows that they can survive in the presence of far-UV radiation, and their formation could even be enhanced due to the radiation. This opens the possibility of detecting complex molecules in other far-UV illuminated regions, such as protoplanetary disks, in the future. From this work we conclude that grain surface chemistry and non-thermal desorption are crucial processes in the ISM and therefore must be incorporated into photochemical models to interpret the observations.

References

1   E. L. Gibb, D. C. B. Whittet, W. A. Schutte, A. C. A. Boogert, J. E. Chiar, P. Ehrenfreund, P. A. Gerakines, J. V. Keane, A. G. G. M. Tielens, E. F. van Dishoeck and O. Kerkhof, *ApJ*, 2000, **536**, 347–356.

2   E. L. Gibb, D. C. B. Whittet, A. C. A. Boogert and A. G. G. M. Tielens, *ApJS*, 2004, **151**, 35–73.

3   A. C. A. Boogert, K. M. Pontoppidan, C. Knez, F. Lahuis, J. Kessler-Silacci, E. F. van Dishoeck, G. A. Blake, J.-C. Augereau, S. E. Bisschop, S. Bottinelli, T. Y. Brooke, J. Brown, A. Crapsi, N. J. Evans, II, H. J. Fraser, V. Geers, T. L. Huard, J. K. Jørgensen, K. I. Öberg, L. E. Allen, P. M. Harvey, D. W. Koerner, L. G. Mundy, D. L. Padgett, A. I. Sargent and K. R. Stapelfeldt, *ApJ*, 2008, **678**, 985–1004.

4   K. M. Pontoppidan, A. C. A. Boogert, H. J. Fraser, E. F. van Dishoeck, G. A. Blake, F. Lahuis, K. I. Öberg, N. J. Evans, II and C. Salyk, *ApJ*, 2008, **678**, 1005–1031.

5   K. I. Öberg, A. C. A. Boogert, K. M. Pontoppidan, G. A. Blake, N. J. Evans, F. Lahuis and E. F. van Dishoeck, *ApJ*, 2008, **678**, 1032–1041.

6   S. Bottinelli, A. C. A. Boogert, J. Bouwman, M. Beckwith, E. F. van Dishoeck, K. I. Öberg, K. M. Pontoppidan, H. Linnartz, G. A. Blake, N. J. Evans, II and F. Lahuis, *ApJ*, 2010, **718**, 1100–1117.

7   A. C. A. Boogert, T. L. Huard, A. M. Cook, J. E. Chiar, C. Knez, L. Decin, G. A. Blake, A. G. G. M. Tielens and E. F. van Dishoeck, *ApJ*, 2011, **729**, 92.

8   R. T. Garrod, *ApJ*, 2013, **765**, 60.

9   J. E. Elsila, J. P. Dworkin, M. P. Bernstein, M. P. Martin and S. A. Sandford, *ApJ*, 2007, **660**, 911–918.

10   D. P. Glavin, A. S. Burton, J. E. Elsila, J. P. Dworkin, Q.-Z. Yin and P. Jenniskens, Lunar and Planetary Institute Science Conference Abstracts, 2013, p. 1189.

11   J. E. Elsila, D. P. Glavin and J. P. Dworkin, *Meteoritics and Planetary Science*, 2009, **44**, 1323–1330.

12   L. E. Snyder, F. J. Lovas, J. M. Hollis, D. N. Friedel, P. R. Jewell, A. Remijan, V. V. Ilyushin, E. A. Alekseev and S. F. Dyubko, *ApJ*, 2005, **619**, 914–930.

13   P. A. Jones, M. R. Cunningham, P. D. Godfrey and D. M. Cragg, *MNRAS*, 2007, **374**, 579–589.

14   M. R. Cunningham, P. A. Jones, P. D. Godfrey, D. M. Cragg, I. Bains, M. G. Burton, P. Calisse, N. H. M. Crighton, S. J. Curran, T. M. Davis, J. T. Dempsey, B. Fulton, M. G. Hidas, T. Hill, L. Kedziora-Chudczer, V. Minier, M. B. Pracy, C. Purcell, J. Shobbrook and T. Travouillon, *MNRAS*, 2007, **376**, 1201–1210.

15   J. M. Hollis, F. J. Lovas and P. R. Jewell, *ApJ*, 2000, **540**, L107–L110.

16   J. M. Hollis, F. J. Lovas, A. J. Remijan, P. R. Jewell, V. V. Ilyushin and I. Kleiner, *ApJ*, 2006, **643**, L25–L28.

17   A. Belloche, K. M. Menten, C. Comito, H. S. P. Müller, P. Schilke, J. Ott, S. Thorwirth and C. Hieret, *A&A*, 2008, **482**, 179–196.

18   A. Belloche, R. T. Garrod, H. S. P. Müller, K. M. Menten, C. Comito and P. Schilke, *A&A*, 2009, **499**, 215–232.

19   P. Hily-Blant, D. Teyssier, S. Philipp and R. Güsten, *A&A*, 2005, **440**, 909–919.

20   J. Pety, D. Teyssier, D. Fossé, M. Gerin, E. Roueff, A. Abergel, E. Habart and J. Cernicharo, *A&A*, 2005, **435**, 885–899.

21   M. Gerin, J. R. Goicoechea, J. Pety and P. Hily-Blant, *A&A*, 2009, **494**, 977–985.

22   V. Guzmán, J. Pety, P. Gratier, J. R. Goicoechea, M. Gerin, E. Roueff and D. Teyssier, *A&A*, 2012, **543**, L1.

23   J. Pety, J. R. Goicoechea, P. Hily-Blant, M. Gerin and D. Teyssier, *A&A*, 2007, **464**, L41–L44.

24   V. V. Guzman, J. R. Goicoechea, J. Pety, P. Gratier, M. Gerin, E. Roueff, F. Le Petit, J. Le Bourlot and A. Faure, *ArXiv e-prints*, 2013.

25   S. E. Cummins, R. A. Linke and P. Thaddeus, *ApJS*, 1986, **60**, 819–878.

26 G. A. Blake, E. C. Sutton, C. R. Masson and T. G. Phillips, *ApJ*, 1987, **315**, 621–645.

27 S. E. Bisschop, J. K. Jørgensen, E. F. van Dishoeck and E. B. M. de Wachter, *A&A*, 2007, **465**, 913–929.

28 E. F. van Dishoeck, G. A. Blake, D. J. Jansen and T. D. Groesbeck, *ApJ*, 1995, **447**, 760.

29 S. Cazaux, A. G. G. M. Tielens, C. Ceccarelli, A. Castets, V. Wakelam, E. Caux, B. Parise and D. Teyssier, *ApJ*, 2003, **593**, L51–L55.

30 E. Herbst and E. F. van Dishoeck, *ARA&A*, 2009, **47**, 427–480.

31 D. Teyssier, D. Fossé, M. Gerin, J. Pety, A. Abergel and E. Roueff, *A&A*, 2004, **417**, 135–149.

32 M. Agúndez, J. Cernicharo, M. Guélin, M. Gerin, M. C. McCarthy and P. Thaddeus, *A&A*, 2008, **478**, L19–L22.

33 J. R. Goicoechea, J. Pety, M. Gerin, D. Teyssier, E. Roueff, P. Hily-Blant and S. Baek, *A&A*, 2006, **456**, 565–580.

34 J. R. Goicoechea, J. Pety, M. Gerin, P. Hily-Blant and J. Le Bourlot, *A&A*, 2009, **498**, 771–783.

35 J. Pety, P. Gratier, V. Guzmán, E. Roueff, M. Gerin, J. R. Goicoechea, S. Bardeau, A. Sievers, F. Le Petit, J. Le Bourlot, A. Belloche and D. Talbi, *A&A*, 2012, **548**, A68.

36 V. Guzmán, J. Pety, J. R. Goicoechea, M. Gerin and E. Roueff, *A&A*, 2011, **534**, A49.

37 P. Gratier, J. Pety, V. Guzmán, M. Gerin, J. R. Goicoechea, E. Roueff and A. Faure, *A&A*, 2013, **557**, A101.

38 K. I. Öberg, M. D. Boamah, E. C. Fayolle, R. T. Garrod, C. J. Cyganowski and F. van der Tak, *ApJ*, 2013, **771**, 95.

39 A. Bacmann, V. Taquet, A. Faure, C. Kahane and C. Ceccarelli, *A&A*, 2012, **541**, L12.

40 H. E. Matthews, P. Friberg and W. M. Irvine, *ApJ*, 1985, **290**, 609–614.

41 W. M. Irvine, P. Friberg, N. Kaifu, K. Kawaguchi, Y. Kitamura, H. E. Matthews, Y. Minh, S. Saito, N. Ukita and S. Yamamoto, *ApJ*, 1989, **342**, 871–875.

42 S. Muller, A. Beelen, M. Guélin, S. Aalto, J. H. Black, F. Combes, S. J. Curran, P. Theule and S. N. Longmore, *A&A*, 2011, **535**, A103.

43 A. A. Penzias and C. A. Burrus, *ARA&A*, 1973, **11**, 51–+.

44 D. A. Neufeld, P. Schilke, K. M. Menten, M. G. Wolfire, J. H. Black, F. Schuller, H. S. P. Müller, S. Thorwirth, R. Güsten and S. Philipp, *A&A*, 2006, **454**, L37–L40.

45 D. A. Neufeld, M. G. Wolfire and P. Schilke, *ApJ*, 2005, **628**, 260–274.

46 P. Sonnentrucker, D. A. Neufeld, T. G. Phillips, M. Gerin, D. C. Lis, M. de Luca, J. R. Goicoechea, J. H. Black, T. A. Bell, F. Boulanger, J. Cernicharo, A. Coutens, E. Dartois, M. Kaźmierczak, P. Encrenaz, E. Falgarone, T. R. Geballe, T. Giesen, B. Godard, P. F. Goldsmith, C. Gry, H. Gupta, P. Hennebelle, E. Herbst, P. Hily-Blant, C. Joblin, R. Kołos, J. Krełowski, J. Martín-Pintado, K. M. Menten, R. Monje, B. Mookerjea, J. Pearson, M. Perault, C. M. Persson, R. Plume, M. Salez, S. Schlemmer, M. Schmidt, J. Stutzki, D. Teyssier, C. Vastel, S. Yu, E. Caux, R. Güsten, W. A. Hatch, T. Klein, I. Mehdi, P. Morris and J. S. Ward, *A&A*, 2010, **521**, L12.

47 M. Asplund, N. Grevesse, A. J. Sauval and P. Scott, *ARA&A*, 2009, **47**, 481–522.

48 T. P. Snow, J. D. Destree and A. G. Jensen, *ApJ*, 2007, **655**, 285–298.

49 V. Guzmán, E. Roueff, J. Gauss, J. Pety, P. Gratier, J. R. Goicoechea, M. Gerin and D. Teyssier, *A&A*, 2012, **548**, A94.

50 A. Fuente, A. Rodríguez-Franco, S. García-Burillo, J. Martín-Pintado and J. H. Black, *A&A*, 2003, **406**, 899–913.

51 O. Berné, C. Joblin, Y. Deville, J. D. Smith, M. Rapacioli, J. P. Bernard, J. Thomas, W. Reach and A. Abergel, *A&A*, 2007, **469**, 575–586.

52 P. Pilleri, J. Montillaud, O. Berné and C. Joblin, *A&A*, 2012, **542**, A69.

53 B. A. McGuire, P. B. Carroll, R. A. Loomis, G. A. Blake, J. M. Hollis, F. J. Lovas, P. R. Jewell and A. J. Remijan, *ArXiv e-prints*, 2013.

54 X. Huang, R. C. Fortenberry and T. J. Lee, *ApJ*, 2013, **768**, L25.

55 R. C. Fortenberry, X. Huang, T. D. Crawford and T. J. Lee, *ApJ*, 2013, **772**, 39.

56 M. P. Bernstein, J. P. Dworkin, S. A. Sandford, G. W. Cooper and L. J. Allamandola, *Nature*, 2002, **416**, 401–403.

57 G. M. Muñoz Caro, U. J. Meierhenrich, W. A. Schutte, B. Barbier, A. Arcones Segovia, H. Rosenbauer, W. H.-P. Thiemann, A. Brack and J. M. Greenberg, *Nature*, 2002, **416**, 403–406.

58 R. T. Garrod, S. L. W. Weaver and E. Herbst, *ApJ*, 2008, **682**, 283–302.

59 J. G. Mangum and A. Wootten, *ApJS*, 1993, **89**, 123–153.

60 S. Leurini, P. Schilke, K. M. Menten, D. R. Flower, J. T. Pottage and L.-H. Xu, *A&A*, 2004, **422**, 573–585.

61 J. G. Mangum, J. Darling, C. Henkel and K. M. Menten, *ApJ*, 2013, **766**, 108.

62 C. R. Purcell, R. Balasubramanyam, M. G. Burton, A. J. Walsh, V. Minier, M. R. Hunt-Cunningham, L. L. Kedziora-Chudczer, S. N. Longmore, T. Hill, I. Bains, P. J. Barnes, A. L. Busfield, P. Calisse, N. H. M. Crighton, S. J. Curran, T. M. Davis, J. T. Dempsey, G. Derragopian, B. Fulton, M. G. Hidas, M. G. Hoare, J.-K. Lee, E. F. Ladd, S. L. Lumsden, T. J. T. Moore, M. T. Murphy, R. D. Oudmaijer, M. B. Pracy, J. Rathborne, S. Robertson, A. S. B. Schultz, J. Shobbrook, P. A. Sparks, J. Storey and T. Travouillion, *MNRAS*, 2006, **367**, 553–576.

63 H. S. P. Müller, S. Thorwirth, D. A. Roth and G. Winnewisser, *A&A*, 2001, **370**, L49–L52.

64 H. M. Pickett, R. L. Poynter, E. A. Cohen, M. L. Delitsky, J. C. Pearson and H. S. P. Müller, *J. Quant. Spec. Radiat. Transf.*, 1998, **60**, 883–890.

65 H. Kim, R. Keller and W. D. Gwinn, *J. Chem. Phys.*, 1962, **37**, 2748–2750.

66 N. B. Hannay and C. P. Smyth, *J Am Chem Soc.*, 1946, **68**, 2408–2409.

67 I. Kleiner, F. J. Lovas and M. Godefroid, *Journal of Physical and Chemical Reference Data*, 1996, **25**, 1113–1210.

68 P. M. Burrell, E. Bjarnov and R. H. Schwendeman, *Journal of Molecular Spectroscopy*, 1980, **82**, 193–201.

69 R. L. Hudson and M. J. Loeffler, *ApJ*, 2013, **773**, 109.

70 M. D. Ward and S. D. Price, *ApJ*, 2011, **741**, 121.

71 J. V. Keane, A. G. G. M. Tielens, A. C. A. Boogert, W. A. Schutte and D. C. B. Whittet, *A&A*, 2001, **376**, 254–270.

72 A. G. G. M. Tielens and W. Hagen, *A&A*, 1982, **114**, 245–260.

73 R. Garrod, I. H. Park, P. Caselli and E. Herbst, *Faraday Discussions*, 2006, **133**, 51.

74 S. Ioppolo, H. M. Cuppen, E. F. van Dishoeck and H. Linnartz, *MNRAS*, 2011, **410**, 1089–1095.

75 V. Vinogradoff, F. Duvernay, G. Danger, P. Theulé, F. Borget and T. Chiavassa, *A&A*, 2013, **549**, A40.

76 F. Mispelaer, P. Theulé, H. Aouididi, J. Noble, F. Duvernay, G. Danger, P. Roubin, O. Morata, T. Hasegawa and T. Chiavassa, *A&A*, 2013, **555**, A13.

77 J. R. Goicoechea, M. Compiègne and E. Habart, *ApJ*, 2009, **699**, L165–L168.

A   Observational tables

Table 4 Observation parameters of the deep integrations of the HCOOH lines detected toward the PDR and dense core.

Molecule	Transition	ν GHz	E_u K	A_{ul} s^{-1}	g_u	Line area $mK\,km\,s^{-1}$	Velocity $km\,s^{-1}$	FWHM $km\,s^{-1}$	T_{peak} mK	RMS mK	Peak S/N
						PDR					
$t-HCOOH$	$4_{14}-3_{13}$	86.546	13.6	6.0×10^{-6}	9	14.3±2.5	10.63	0.41	32.6	6.0	5
$t-HCOOH$	$4_{04}-3_{03}$	89.579	10.8	7.0×10^{-6}	9	13.9±2.6	10.74	0.58	22.6	5.8	4
$t-HCOOH$	$4_{22}-3_{21}$	90.165	23.5	6.0×10^{-6}	9	10.2±2.2	10.91	0.51	18.7	5.4	3
$t-HCOOH$	$4_{13}-3_{12}$	93.098	14.4	8.0×10^{-6}	9	10.8±2.4	10.54	0.51	19.7	6.0	3
$t-HCOOH$	$5_{15}-4_{14}$	108.127	18.8	1.3×10^{-5}	11	11.3±2.9	10.83	0.38	27.7	9.8	3
$t-HCOOH$	$5_{05}-4_{04}$	111.747	16.1	1.4×10^{-5}	11	13.2±5.1	10.82	0.41	30.0	9.3	3
$t-HCOOH$	$6_{16}-5_{15}$	129.672	25.0	2.2×10^{-5}	13	17.8±4.1	10.66	0.40	42.1	13.2	3
$t-HCOOH$	$6_{06}-5_{05}$	133.767	22.5	2.5×10^{-5}	13	17.1±3.9	10.57	0.36	45.2	14.1	3
$t-HCOOH$	$6_{24}-5_{23}$	135.738	35.4	2.3×10^{-5}	13	16.1±3.5	10.46	0.30	49.9	13.9	4
						CORE					
$t-HCOOH$	$4_{04}-3_{03}$	89.579	10.8	7.0×10^{-6}	9	17.2±2.8	10.56	0.59	27.4	6.2	4
$t-HCOOH$	$4_{13}-3_{12}$	93.098	14.4	8.0×10^{-6}	9	11.4±2.6	10.64	0.34	31.4	6.5	5
$t-HCOOH$	$5_{15}-4_{14}$	108.127	18.8	1.3×10^{-5}	11	16.3±3.5	10.61	0.38	40.1	9.9	4
$t-HCOOH$	$5_{05}-4_{04}$	111.747	16.1	1.4×10^{-5}	11	11.5±3.1	10.54	0.30	36.3	9.0	4
$t-HCOOH$	$6_{06}-5_{05}$	133.767	22.5	2.5×10^{-5}	13	26.2±5.6	10.39	0.44	55.9	13.5	4

Note: All temperatures are given in the main beam temperature scale.

Table 5 Observation parameters of the deep integrations of the CH_2CO lines detected toward the PDR and dense core.

Molecule	Transition	ν GHz	E_u K	A_{ul} s^{-1}	g_u	Line area $mK\,km\,s^{-1}$	Velocity $km\,s^{-1}$	FWHM $km\,s^{-1}$	T_{peak} mK	RMS mK	Peak S/N
						PDR					
$o-CH_2CO$	$4_{13}-3_{12}$	81.586	22.9	5.0×10^{-6}	27	83.1±10.7	10.62	0.69	113.4	19.8	6
$o-CH_2CO$	$5_{15}-4_{14}$	100.095	27.5	1.0×10^{-5}	33	87.9± 3.6	10.70	0.64	128.7	7.4	17
$o-CH_2CO$	$5_{14}-4_{13}$	101.981	27.8	1.1×10^{-5}	33	89.0± 3.2	10.67	0.65	127.7	7.1	18
$o-CH_2CO$	$7_{17}-6_{16}$	140.127	40.0	2.9×10^{-5}	45	77.9± 4.7	10.66	0.55	133.0	12.4	11
$o-CH_2CO$	$7_{16}-6_{15}$	142.769	40.5	3.1×10^{-5}	45	68.4± 8.1	10.66	0.47	135.3	25.6	5
$o-CH_2CO$	$8_{18}-7_{17}$	160.142	47.6	4.5×10^{-5}	51	102.7±13.5	10.74	0.72	134.2	35.7	4
$o-CH_2CO$	$10_{19}-9_{18}$	203.940	66.9	9.3×10^{-5}	63	45.9± 7.0	10.72	0.67	64.8	10.6	6
$p-CH_2CO$	$5_{05}-4_{04}$	101.037	14.5	1.1×10^{-5}	11	45.3± 3.1	10.81	0.70	60.8	6.8	9
$p-CH_2CO$	$7_{07}-6_{06}$	141.438	27.2	3.1×10^{-5}	15	42.9± 6.7	10.67	0.56	71.6	17.9	4
$o-CH_2CO^c$	$5_{33}-4_{32}{}^a$	101.002	132.8	7.0×10^{-6}	33	31.0± 4.5	10.98	0.87	33.6	8.5	4
$o-CH_2CO^c$	$7_{35}-6_{34}{}^b$	141.402	145.4	2.5×10^{-5}	45	50.2± 8.0	10.28	1.03	45.9	16.9	3
$o-CH_2CO^c$	$7_{25}-6_{24}$	141.452	79.5	2.8×10^{-5}	15	39.1± 6.9	10.48	0.83	44.4	15.7	3
						CORE					
$o-CH_2CO$	$4_{13}-3_{12}$	81.586	22.9	5.0×10^{-6}	27	34.3±8.6	10.86	0.69	47.0	17.8	3
$o-CH_2CO$	$5_{15}-4_{14}$	100.095	27.5	1.0×10^{-5}	33	38.9±3.3	10.67	0.52	70.7	7.8	9
$o-CH_2CO$	$5_{14}-4_{13}$	101.981	27.8	1.1×10^{-5}	33	33.3±3.2	10.65	0.47	66.6	7.8	9
$o-CH_2CO$	$7_{17}-6_{16}$	140.127	40.0	2.9×10^{-5}	45	30.6±4.2	10.60	0.51	56.5	11.8	5
$p-CH_2CO$	$5_{05}-4_{04}$	101.037	14.5	1.1×10^{-5}	11	29.5±3.9	10.68	0.73	37.7	8.0	5
$p-CH_2CO$	$7_{07}-6_{06}$	141.438	27.2	3.1×10^{-5}	15	31.1±7.0	10.68	0.69	42.5	17.0	3

Note: All temperatures are given in the main beam temperature scale.
[a] Blended with the $5_{32}-4_{31}$ line.
[b] Blended with the $7_{34}-6_{33}$ line.
[c] The line identification is uncertain.

Table 6 Observation parameters of the deep integrations of the CH_3CHO lines detected toward the PDR and dense core.

Molecule	Transition	ν GHz	E_u K	A_{ul} s^{-1}	g_u	Line area mK km s^{-1}	Velocity km s^{-1}	FWHM km s^{-1}	T_{peak} mK	RMS mK	Peak S/N
						PDR					
$CH_3CHO - E$	$5_{15} - 4_{14}$	93.595	15.8	2.5×10^{-5}	22	57.5 ± 2.5	10.75	0.63	86.0	5.2	16
$CH_3CHO - E$	$5_{05} - 4_{04}$	95.947	13.9	2.8×10^{-5}	22	81.6 ± 3.0	10.67	0.68	113.5	6.1	19
$CH_3CHO - E$	$5_{14} - 4_{13}$	98.863	16.6	3.0×10^{-5}	22	68.2 ± 3.5	10.68	0.61	104.7	8.0	13
$CH_3CHO - E$	$6_{16} - 5_{15}$	112.254	21.2	4.5×10^{-5}	26	41.8 ± 4.1	10.59	0.47	83.4	11.1	8
$CH_3CHO - E$	$6_{06} - 5_{05}$	114.940	19.4	5.2×10^{-5}	26	88.2 ± 15.3	10.65	0.67	124.3	32.0	4
$CH_3CHO - E$	$7_{07} - 6_{06}$	133.831	25.9	8.2×10^{-5}	30	36.2 ± 7.4	10.70	0.83	41.0	16.6	2
$CH_3CHO - E$	$7_{16} - 6_{15}$	138.285	28.9	8.6×10^{-5}	30	30.6 ± 4.7	10.60	0.52	54.9	14.5	4
$CH_3CHO - E$	$8_{18} - 7_{17}$	149.505	34.7	1.1×10^{-4}	34	20.5 ± 4.2	10.81	0.33	59.1	16.8	4
$CH_3CHO - A$	$5_{15} - 4_{14}$	93.581	15.7	2.5×10^{-5}	22	44.3 ± 2.6	10.66	0.54	76.9	6.0	13
$CH_3CHO - A$	$5_{05} - 4_{04}$	95.963	13.8	2.8×10^{-5}	22	73.1 ± 2.8	10.70	0.63	108.5	5.8	19
$CH_3CHO - A$	$5_{24} - 4_{23}$	96.274	22.9	2.4×10^{-5}	22	13.5 ± 2.3	10.55	0.48	26.7	5.6	5
$CH_3CHO - A$	$5_{23} - 4_{22}$	96.633	23.0	2.4×10^{-5}	22	12.3 ± 1.9	10.68	0.41	28.5	5.1	6
$CH_3CHO - A$	$5_{14} - 4_{13}$	98.901	16.5	3.0×10^{-5}	22	73.8 ± 3.4	10.73	0.62	112.7	7.7	15
$CH_3CHO - A$	$6_{16} - 5_{15}$	112.249	21.1	4.5×10^{-5}	26	56.0 ± 5.1	10.68	0.69	76.3	11.4	7
$CH_3CHO - A$	$6_{06} - 5_{05}$	114.960	19.4	5.0×10^{-5}	26	83.6 ± 13.6	10.71	0.67	117.5	28.8	4
$CH_3CHO - A$	$7_{07} - 6_{06}$	133.854	25.8	7.9×10^{-5}	30	30.8 ± 3.6	10.61	0.39	73.9	11.9	6
$CH_3CHO - A$	$7_{25} - 6_{24}$	135.685	35.0	7.9×10^{-5}	30	15.4 ± 3.2	10.76	0.29	50.5	13.2	4
$CH_3CHO - A$	$7_{16} - 6_{15}$	138.320	28.8	8.6×10^{-5}	30	52.9 ± 6.8	10.74	0.49	100.6	17.0	6
						CORE					
$CH_3CHO - E$	$5_{15} - 4_{14}$	93.595	15.8	2.5×10^{-5}	22	34.4 ± 2.2	10.71	0.74	43.5	4.2	10
$CH_3CHO - E$	$5_{05} - 4_{04}$	95.947	13.9	2.8×10^{-5}	22	38.5 ± 2.4	10.66	0.63	57.1	5.4	10
$CH_3CHO - E$	$5_{14} - 4_{13}$	98.863	16.6	3.0×10^{-5}	22	26.6 ± 4.0	10.63	0.60	41.5	8.8	5
$CH_3CHO - A$	$5_{15} - 4_{14}$	93.581	15.7	2.5×10^{-5}	22	26.7 ± 2.0	10.62	0.57	44.1	4.6	10
$CH_3CHO - A$	$5_{05} - 4_{04}$	95.963	13.8	2.8×10^{-5}	22	33.1 ± 3.1	10.67	0.80	38.9	5.7	7
$CH_3CHO - A$	$5_{14} - 4_{13}$	98.901	16.5	3.0×10^{-5}	22	35.5 ± 5.7	10.74	0.74	44.8	9.5	5
$CH_3CHO - A$	$6_{16} - 5_{15}$	112.249	21.1	4.5×10^{-5}	26	16.0 ± 3.5	10.62	0.55	27.2	9.9	3

Note: All temperatures are given in the main beam temperature scale.

Table 7 Observation parameters of the deep integrations of the CH_3CCH lines detected toward the PDR and dense core.

Molecule	Transition	ν GHz	E_u K	A_{ul} s^{-1}	g_u	Line area mK km s^{-1}	Velocity km s^{-1}	FWHM^a km s^{-1}	T_{peak} mK	RMS mK	Peak S/N
						PDR					
$CH_3CCH - E$	$5_1 - 4_1$	85.456	19.5	5.93×10^{-7}	22	15.2 ± 2.7	10.54	0.60	23.9	6.8	3
$CH_3CCH - E$	$6_1 - 5_1$	102.546	24.4	1.05×10^{-6}	26	16.0 ± 2.7	10.95	0.60	25.0	7.6	3
$CH_3CCH - E$	$8_1 - 7_1$	136.725	36.7	2.50×10^{-6}	34	16.8 ± 3.7	10.53	0.60	26.3	12.2	2
$CH_3CCH - E$	$12_1 - 11_1$	205.077	71.2	8.95×10^{-6}	50	22.3 ± 3.7	10.67	0.60	34.9	7.6	4
$CH_3CCH - E$	$13_1 - 12_1$	222.163	81.9	1.14×10^{-5}	27	15.3 ± 3.8	10.66	0.60	23.9	7.9	3
$CH_3CCH - A$	$5_0 - 4_0$	85.457	12.3	6.18×10^{-7}	22	14.6 ± 2.3	10.77	0.60	22.8	5.7	4
$CH_3CCH - A$	$6_0 - 5_0$	102.548	17.2	1.08×10^{-6}	26	10.8 ± 2.7	10.72	0.60	17.0	7.1	2
$CH_3CCH - A$	$8_3 - 7_3$	136.705	94.6	2.25×10^{-6}	34	15.2 ± 3.7	10.55	0.60	23.8	11.8	2
$CH_3CCH - A$	$12_0 - 11_0$	205.081	64.0	9.02×10^{-6}	50	22.0 ± 4.0	10.76	0.60	34.4	7.9	4
$CH_3CCH - A$	$13_0 - 12_0$	222.167	74.6	1.15×10^{-5}	27	14.1 ± 3.7	10.35	0.60	22.1	7.6	2
$CH_3CCH - A$	$14_3 - 13_3$	239.211	151.1	9.96×10^{-5}	58	28.6 ± 5.9	10.46	0.60	44.8	12.8	3
$CH_3CCH - A$	$14_0 - 13_0$	239.252	86.1	1.40×10^{-5}	58	54.2 ± 7.5	10.63	0.60	84.9	16.1	5
						CORE					
$CH_3CCH - E$	$5_1 - 4_1$	85.456	19.5	5.93×10^{-7}	22	13.5 ± 1.9	10.48	0.50	25.4	5.5	4
$CH_3CCH - E$	$6_1 - 5_1$	102.546	24.4	1.05×10^{-6}	26	20.0 ± 2.9	10.48	0.50	37.6	8.9	4
$CH_3CCH - E$	$8_1 - 7_1$	136.725	36.7	2.50×10^{-6}	34	27.4 ± 4.0	10.56	0.50	51.6	14.2	3
$CH_3CCH - A$	$5_0 - 4_0$	85.457	12.3	6.18×10^{-7}	22	16.8 ± 2.4	10.59	0.50	31.5	6.3	4
$CH_3CCH - A$	$6_0 - 5_0$	102.548	17.2	1.08×10^{-6}	26	25.7 ± 2.8	10.74	0.50	48.2	8.5	5

Note: All temperatures are given in the main beam temperature scale.
^{a} The line width was fixed to guide the Gaussian fit at low signal-to-noise ratio.

Faraday Discussions Accepted Manuscript